Renewable Energy 70 (2014) 11–23

Contents lists available at ScienceDirect

Renewable Energy

journal homepage: www.elsevier.com/locate/renene

Effect of downwind swells on offshore wind energy harvesting – A large-eddy simulation study

Di Yang [a,b], Charles Meneveau [a,b], Lian Shen [c,d,*]

[a] Department of Mechanical Engineering, Johns Hopkins University, Baltimore, MD 21218, USA
[b] Center for Environmental and Applied Fluid Mechanics, Johns Hopkins University, Baltimore, MD 21218, USA
[c] Department of Mechanical Engineering, University of Minnesota, Minneapolis, MN 55455, USA
[d] St. Anthony Falls Laboratory, University of Minnesota, Minneapolis, MN 55414, USA

ARTICLE INFO

Article history:
Received 28 September 2013
Accepted 28 March 2014
Available online 3 May 2014

Keywords:
Offshore wind energy
Swell
Wind–wave interaction
Large-eddy simulation
Turbulence

ABSTRACT

The effect of ocean downwind swells on the harvesting of offshore wind energy is studied using large-eddy simulation of fully developed wind turbine array boundary layers, which is dynamically coupled with high-order spectral simulation of sea-surface wave field with and without the presence of a downwind swell. For the two moderate wind speeds of 7 m/s and 10 m/s considered in this study, the swell is found to induce a temporal oscillation in the extracted wind power at the swell frequency, with a magnitude of 6.7% and 4.0% of the mean wind power output, respectively. Furthermore, the averaged wind power extraction is found to be increased by as much as 18.8% and 13.6%, respectively. Statistical analysis of the wind field indicates that the wind speed in the lower portion of the boundary layer oscillates periodically with fast wind above the swell trough and slow wind above the swell crest, resulting in the observed wind power oscillation. The wind above the swell accelerates due to the strong wave forcing, causes a net upward flux of kinetic energy into the wind turbine layer, and thus acts to increase the extracted wind power of the turbines. For a high wind speed of 17 m/s, the wave-induced motion becomes relatively weak and the swell effect on the wind turbine performance diminishes.

1. Introduction

With more available space, faster winds, and smaller visual impact and noise, offshore wind power has become a promising direction for wind energy and associated research. Offshore wind farms operate in a complex environment in which the sea surface is characterized by progressive waves of various sizes that interact with the wind over a wide range of scales. Therefore, the understanding of offshore wind farm dynamics and the predictions of wind turbine performance critically depend on the complex interaction among wind turbines, wind, and waves.

Previous studies on marine atmospheric boundary layer have shown that the characteristics of offshore wind are highly affected by its interaction with the sea-surface waves [1–4]. Among various types of sea-surface waves, the ocean swells play a distinct role. Generated by storms far away, swells can travel over long distance, enter the site of offshore wind farm, and mix with the local wind-seas (i.e., the wave field generated by the local wind). Because of the large amplitude and fast propagation speed, swells are capable of imposing strong disturbance to the marine wind field [3,5–7] and even generating wind under low and moderate wind conditions [8–10]. Thus, better understanding of turbine wake dynamics in offshore wind farms requires consideration of swell effect on wind.

In recent years, the combination of large-eddy simulation (LES) of atmospheric boundary layer and proper wind turbine models has made LES a useful tool for wind energy research [11–14]. For example, by performing LES of an "infinite" wind turbine array boundary layer, Calaf et al. [15] were able to capture the complex turbulent flow within a large wind farm as well as its expected interaction with the atmospheric boundary layer at large scales. Their LES results showed that inside a fully developed wind turbine array boundary layer, the wind field is energized for downstream wind energy harvesting through the vertical flux of kinetic energy from the atmosphere above.

While wind power on land is being actively explored, there has been a lack of LES tools for the simulation of offshore wind farms. Recently, a hybrid numerical capability has been developed by

* Corresponding author. Department of Mechanical Engineering, University of Minnesota, Minneapolis, MN 55455, USA. Tel.: +1 612 625 7527.
E-mail address: shen@umn.edu (L. Shen).

http://dx.doi.org/10.1016/j.renene.2014.03.069
0960-1481/

Yang et al. [16] for the simulation of large-scale offshore wind farms. The numerical framework consists of a LES of wind turbine array boundary layers on a curvilinear coordinate that follows the wave surface motion [17], and a spectral simulation of nonlinear sea-surface waves based on potential flow theory. The wind and wave simulations are dynamically coupled [18]. This simulation tool was shown to capture the effects of a broadband sea-surface wave field on the offshore wind farm dynamics [16]. In this study, we apply this hybrid simulation tool to study cases when swells are present.

In our simulation, a domain of 2.1 km long, 1.5 km wide, and 1.0 km high is considered. A 3 × 3 wind turbine array (aligned in both rows and columns) with periodic boundary conditions in the horizontal directions is used to model a fully developed "infinite" turbine array boundary layer [15,19–24], under neutral stratification. We note that some of the previous studies also considered wind turbine arrays with staggered or oblique arrangement, and found appreciable effect of the layout pattern on the performance of land-based wind farms [19,23,24]. Similar turbine array layout effect is expected for offshore wind farms. However, the presence of ocean swells is expected to induce qualitatively similar distortion on the wind field as the leading order effect for both the aligned and staggered turbines offshore. As a first attempt on investigating the swell effect, we focus on the aligned turbine array that has been used as the baseline case in most of the previous LES studies. The wind turbine effect is modeled by the actuator-disk model [11,12] with the effect of the turbine tower neglected as in most of the previous studies [15,19–22,24]. Among practical designs, many highly stable floating turbine platforms have only small motions under wind and wave forcing [e.g. Refs. [25,26]]. Although these small motions are still crucial for analyzing the structural response of the turbine system, they are not expected to induce significant effect on wind power generation. In this study, we focus on this type of highly stable platforms as a first step of the investigation, and thus treat the turbines as fixed in space (and as a result, the effect of mooring cables is also neglected).

Three different wind speeds, $U_{top} = 7.0$, 10.0, and 17.0 m/s (where U_{top} is the mean wind speed at the top of the simulation domain, 1.0 km above the mean sea surface), are considered. The sea surface has a broadband wave field. In addition, a swell propagating downwind is considered. In the simulation domain that is 2.1 km long, there are nine waves in the monochromatic swell train propagating in the streamwise direction, corresponding to a moderate wavelength of $\lambda_s = 233.3$ m. A typical steepness of $2\pi a_s/\lambda_s = 0.1$ is considered [4,9,27–29] so that the swell amplitude is $a_s = 3.7$ m. We remark that the problem can be further complicated by the fact that a swell can propagate in a different direction with respect to the local wind-seas. As the first attempt on the study of swell effect on offshore wind farms, we focus on the downwind swell condition that was investigated the most as a canonical problem in previous studies on wind–wave interaction [e.g. Refs. [8–10,30]].

Based on the simulation data, the effect of the downwind swell on the wind power extraction rate of the turbines is studied, with a focus on the swell-induced change in the mean value as well as temporal fluctuations. Statistical analysis of the offshore wind turbine array boundary layer is also performed to help understand the physical mechanism responsible for the swell effect.

This paper is organized as follows. First, the numerical method used in our hybrid model is introduced in Section 2, followed by an introduction on the problem setup and the parameters of the simulation cases. Next, the simulation results and data analysis are presented in Section 3 to show the swell effect on wind farm dynamics. Finally, conclusions are given in Section 4.

2. Numerical method

2.1. Large-eddy simulation of wind turbulence

Fig. 1 shows two typical examples of the instantaneous flow field in the offshore wind turbine array boundary layer obtained by the current simulation. In this study, we consider a neutrally stratified atmospheric boundary layer flow for the wind field. In LES, the motion of wind turbulence is described by the filtered Navier–Stokes equations for incompressible flows

$$\frac{\partial \tilde{u}_i}{\partial t} + \tilde{u}_j \frac{\partial \tilde{u}_i}{\partial x_j} = -\frac{1}{\rho_a}\frac{\partial \tilde{p}^*}{\partial x_i} - \frac{\partial \tau_{ij}^d}{\partial x_j} - \frac{1}{\rho_a}\frac{\partial p_\infty}{\partial x}\delta_{i1} + f_T\delta_{i1}, \tag{1}$$

$$\frac{\partial \tilde{u}_i}{\partial x_i} = 0. \tag{2}$$

As shown in Fig. 1, the coordinates are denoted as $x_i(i = 1,2,3) = (x,y,z)$, where x and y are the horizontal coordinates and z is the vertical coordinate, with $z = 0$ being the mean sea surface. The velocity components in x-, y-, and z-directions are denoted as $u_i(i = 1,2,3) = (u,v,w)$, respectively. In Eqs. (1) and (2), $\widetilde{(\ldots)}$ indicates filtering at the grid scale Δ; ρ_a is the density of air; $\tau_{ij} = \widetilde{u_i u_j} - \tilde{u}_i\tilde{u}_j$ is the subgrid-scale (SGS) stress tensor, and τ_{ij}^d is its trace-free part; and $\tilde{p}^* = \tilde{p} + \tau_{kk}/3 - p_\infty$ is the filtered modified pressure. In this study, we consider the condition of mean wind being perpendicular to the wind turbine rotor plane, i.e. along the $+x$-direction. The imposed pressure gradient $\partial p_\infty/\partial x$ models the effect of geostrophic wind forcing [15].

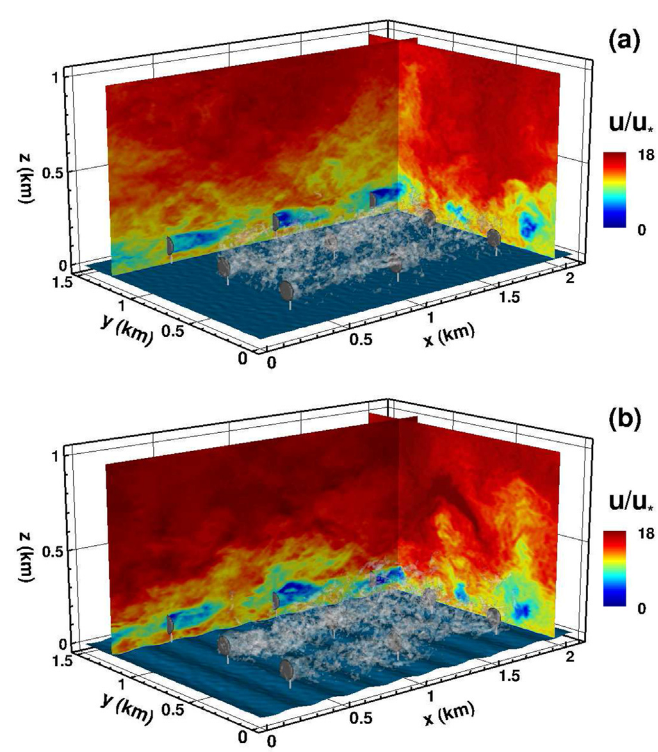

Fig. 1. Flow field in a fully developed wind turbine array boundary layer at sea for $U_{top} = 10$ m/s with: (a) pure wind-seas; and (b) wind-seas mixed with swells. Contours of instantaneous streamwise velocity u (normalized by u_*) are plotted on two representative (x,z)- and (y,z)-planes. The turbulent wakes behind the first four wind turbines are illustrated by the iso-surface of the normalized vorticity magnitude $|\omega|/(u_*/D) = 20$. Here, U_{top} is the mean wind velocity at the top of the simulation domain; u_* is the wind friction velocity above the turbine array; ω is the vorticity; and D is the turbine rotor diameter.

In this study, we consider moderate-amplitude swells, which are mixed with broadband three-dimensional wind-seas. Many practical designs of floating offshore wind turbine platforms, e.g., the MIT/NREL TLP [25] and the WindFloat [26], have only small motions in response to the wind and waves. In this study, we focus on this class of turbine platforms and thus treat them as fixed in space. Associated with the fixed platform, the dynamics of mooring cables is not considered, which should be taken into account if the platform has non-negligible oscillations. The turbine-induced force in Eq. (1), f_T, is calculated by the actuator-disk model originally applied in LES by Jimenez et al. [11,12]. In the present study, we use the modified version proposed by Meyers and Meneveau [19]. In this model, the turbine-induced force per unit mass in the streamwise direction is given by

$$f_T(x_l, y_m, z_n) = -\frac{1}{2} C_T' \left\langle u^T \right\rangle_d^2 \frac{\gamma_{m,n}}{\Delta x}. \quad (3)$$

Here, (x_l, y_m, z_n) denotes the position of a given grid point with index (l,m,n); $C_T' = C_T/(1-a)^2$ is the effective thrust coefficient [15], where C_T is the thrust coefficient and a is the axial induction factor [31]; $\langle u^T \rangle_d$ is the local reference wind velocity evaluated by spatial averaging over all grid points within the turbine disk; $\gamma_{m,n}$ is the fraction of area overlap between the grid cell (m,n) and the turbine rotor circle; and Δx is the streamwise grid size. The effects of wind turbine yaw controller and blade pitch controller are neglected in this actuator-disk model. Note that if the floating platform has non-negligible motion, the current actuator-disk model in Eq. (3) can be generalized by replacing the streamwise velocity $\langle u^T \rangle_d$ with the incident axial wind velocity relative to the wind turbine disk (i.e. including both incoming wind velocity and wind turbine motion). The effects of the turbine tower and nacelle are relatively small and are not considered in this study [also see e.g. Refs. [15,19–22,24]].

We remark that as shown by Meyers and Meneveau [19], the effective thrust coefficient can also be written as $C_T' = [4a/(1-a)][1 + (C_D/C_L)(2/\lambda_t)]$, where C_D and C_L are the drag and lift coefficients of the turbine blade, respectively, and λ_t is the tip-speed ratio. In practice, by means of pitch control, a fixed value for C_T' may be obtained for the range of wind speeds considered here. For clarity of analysis and discussion, in this study we use a fixed value for the effective thrust coefficient, $C_T' = 4/3$, corresponding to the typical values of $C_T = 3/4$ for the thrust coefficient [11] and $a = 1/4$ for the induction factor [19]. The same value of C_T' has been used in several previous LES studies [15,16,19,21,22].

In Eq. (1), the SGS stress tensor is modeled using a Lagrangian-averaged scale-dependent dynamic Smagorinsky model, as described in Bou-Zeid et al. [32]. On the other hand, the molecular viscous term is neglected because the Reynolds number for the flows considered in this study is very high. This omission prevents the resolving of the viscous sub-layer near the wave surface. Consequently, in the simulation, an equilibrium surface-layer model is employed to impose proper sea-surface stress to the wind turbulence, which is expressed as [9,32,33]

$$\tau_{i3}^{SGS}(x,y,t) = -\left[\frac{\kappa}{\ln(d_2/z_0)}\right]^2 \widehat{\widetilde{U}}_r(x,y,t) \times \left[\widehat{\widetilde{u}}_{r,i}(x,y,t)\cos\theta_i + \widehat{\widetilde{u}}_{r,3}(x,y,t)\sin\theta_i\right], \quad i = 1,2. \quad (4)$$

Here, $\kappa = 0.4$ is the von Kármán constant; $\widehat{(\ldots)}$ indicates filtering at the test-filter scale 2Δ; z_0 is the sea-surface roughness associated with the SGS waves; $\theta_i (i = 1,2)$ are the local inclination angles of the wave surface in x_i-direction, with

$$\cos\theta_i = \frac{1}{\sqrt{1 + \left(\partial\tilde{\eta}/\partial x_i\right)^2}}, \quad (5)$$

and

$$\sin\theta_i = \frac{\partial\tilde{\eta}/\partial x_i}{\sqrt{1 + \left(\partial\tilde{\eta}/\partial x_i\right)^2}}, \quad (6)$$

where $\tilde{\eta}(x,y,t)$ is the filtered instantaneous wave surface elevation; $\widehat{\widetilde{u}}_{r,i} (i = 1,2,3)$ are the test-filtered wind velocities relative to the water surface at the first off-surface grid point (which is at height d_2 above the sea surface in the LES code)

$$\widehat{\widetilde{u}}_{r,i}(x,y,t) = \widehat{\widetilde{u}}_i(x,y,d_2,t) - \widehat{\widetilde{u}}_{s,i}(x,y,t), \quad i = 1,2,3. \quad (7)$$

In the above equation, the values of $\widehat{\widetilde{u}}_{s,i}$ are obtained by the test-filtering of the sea-surface velocities $u_{s,i}$ (details for the calculation of $u_{s,i}$ are given in Section 2.3). In Eq. (4)

$$\widehat{\widetilde{U}}_r(x,y,t) = \sqrt{\sum_{i=1}^{2}\left[\widehat{\widetilde{u}}_{r,i}(x,y,t)\cos\theta_i + \widehat{\widetilde{u}}_{r,3}(x,y,t)\sin\theta_i\right]^2} \quad (8)$$

is the magnitude of horizontal wind velocity relative to the wave surface.

In the simulations, the streamwise and spanwise boundaries are treated as periodic, so that the finite number of wind turbines in the simulation domain represent a subset of an infinitely large wind farm [15]. The top of the simulation domain is considered to be rigid and free-slip. The bottom is bounded by the wave surface, with a known tangential stress expressed in terms of the velocity field by Eq. (4). A time-dependent boundary-fitted grid is used to follow the curvature of the wave surface. The irregular wave surface-bounded domain in the physical space is transformed to a right rectangular prism in the computational space using an algebraic mapping [17].

For spatial discretization, we use a Fourier-series-based pseudo-spectral method on a collocated grid in the horizontal directions, and a second-order finite-difference method on a staggered grid in the vertical direction. The governing equations are integrated in time with a fractional-step method as follows: first, the momentum equations without the pressure terms are advanced in time with a second-order Adams–Bashforth scheme; then, a Poisson equation is solved for the pressure to provide correction for the velocity field so that the incompressibility constraint is satisfied. The effect of resolved-scale sea-surface waves on the wind field, i.e. the form drag, is captured by the wave-correlated pressure field. The details and validations of the numerical scheme for solving the Navier–Stokes equations in a curvilinear coordinate system are provided in Yang and Shen [17,34,35]. The details and validations of the LES wind turbulence solver can be found in Yang et al. [36] and Liu et al. [37]. The actuator-disk turbine model in our LES has been tested through simulations of single turbine and turbine array, and the comparisons with measurements, theories, and other LES results show good agreement [16].

2.2. High-order spectral method for the simulation of sea-surface waves

The nonlinear sea-surface wave field is directly simulated using the high-order spectral method (HOSM) [38], which has been successfully applied to the study of various ocean wave problems

[39–42]. The HOSM simulates nonlinear waves using the Zakharov formulation [43], in which the wave motion is described by the surface elevation η and the surface potential Φ^s. Here, $\Phi^s = \Phi(x,y,z=\eta(x,y,t),t)$ with Φ being the velocity potential. With a perturbation series of Φ with respect to the wave steepness to the order of M and a Taylor series expansion about the mean water level $z = 0$

$$\Phi^s(x,y,t) = \sum_{m=1}^{M} \sum_{\ell=0}^{M-m} \frac{\eta^\ell}{\ell!} \frac{\partial^\ell}{\partial z^\ell} \Phi^{(m)}(x,y,z,t)\bigg|_{z=0}, \tag{9}$$

and an eigenfunction expansion of each $\Phi^{(m)}$ with N modes

$$\Phi^{(m)}(x,y,z,t) = \sum_{k=1}^{N} \Phi_k^{(m)}(t) \Psi_k(x,y,z), \tag{10}$$

the kinematic and dynamic free surface boundary conditions are written as [38]

$$\frac{\partial \eta}{\partial t} = -\nabla_h \eta \cdot \nabla_h \Phi^s + \left(1 + |\nabla_h \eta|^2\right) \times \left[\sum_{m=1}^{M} \sum_{\ell=0}^{M-m} \frac{\eta^\ell}{\ell!} \sum_{k=1}^{N} \Phi_k^{(m)} \frac{\partial^{\ell+1} \Psi_k}{\partial z^{\ell+1}}\bigg|_{z=0} \right], \tag{11}$$

$$\frac{\partial \Phi^s}{\partial t} = -g\eta - \frac{|\nabla_h \Phi^s|^2}{2} - \frac{p_a(x,y,t)}{\rho_w} + \frac{1 + |\nabla_h \eta|^2}{2} \times \left[\sum_{m=1}^{M} \sum_{\ell=0}^{M-m} \frac{\eta^\ell}{\ell!} \sum_{k=1}^{N} \Phi_k^{(m)} \frac{\partial^{\ell+1} \Psi_k}{\partial z^{\ell+1}}\bigg|_{z=0} \right]^2. \tag{12}$$

Here, $\nabla_h = (\partial/\partial x, \partial/\partial y)$ is the horizontal gradient; g is the gravitational acceleration; p_a is the air pressure at the wave surface; ρ_w is the density of water; and the operator '$\cdot$' denotes the dot product of two vectors. In this paper, we consider deep water waves, for which the eigenfunctions Ψ_k are

$$\Psi_k(x,y,z) = \exp(|\mathbf{k}|z + i\mathbf{k}\cdot\mathbf{x}). \tag{13}$$

Here, $i = \sqrt{-1}$; and $\mathbf{k} = (k_x, k_y)$ is the wavenumber vector, which is related to the scalar wavenumber k through $k = |\mathbf{k}| = \sqrt{k_x^2 + k_y^2}$.

In HOSM, Eqs. (11) and (12) are advanced in time by a fourth-order Runge–Kutta scheme. The equations are discretized in space by a Fourier-series-based pseudo-spectral method. The nonlinear terms are de-aliased with the 3/2 rule. A complete review of the HOSM (including methodology, validation, and representative applications) is given in Mei et al. [44].

2.3. Coupling of LES of wind and HOSM simulation of waves

The LES of wind turbulence and HOSM simulation of sea-surface wave field are coupled using a fractional-step scheme. At each timestep, first the HOSM simulation advances the wave field to the next timestep using the surface air pressure p_a obtained from LES at the previous timestep. With the updated sea-surface elevation η as well as potential functions Φ^s and Φ, the sea-surface wave orbital velocities are obtained as [38]

$$u_{s,1}(x,y,t) = \frac{\partial \Phi^s}{\partial x} - \frac{\partial \eta}{\partial x} \frac{\partial \Phi}{\partial z}\bigg|_{z=\eta}, \tag{14}$$

$$u_{s,2}(x,y,t) = \frac{\partial \Phi^s}{\partial y} - \frac{\partial \eta}{\partial y} \frac{\partial \Phi}{\partial z}\bigg|_{z=\eta}, \tag{15}$$

$$u_{s,3}(x,y,t) = \frac{\partial \Phi}{\partial z}\bigg|_{z=\eta}. \tag{16}$$

Eqs. (14)–(16) are then used in Eq. (7) to calculate the relative wind velocity with respect to the wave surface motion, which is used in the surface-layer model in Eq. (4). The LES of wind turbulence then advances in time to the next timestep. The above time advancement procedure is repeated for every timestep, so that the wind and wave fields are dynamically coupled in the simulation. Details and validations of the coupling scheme are given in Yang and Shen [18].

2.4. Configuration of simulation

For the simulation of offshore wind farms, we consider a turbulent wind turbine array boundary layer over an open sea area. The computational domain of the LES has a size of $(L_x, L_y, \overline{H}) = (2.1, 1.5, 1.0)$ km, where L_x and L_y are respectively the streamwise and spanwise domain length, and $\overline{H}$ is the height from the top boundary to the mean sea-surface level. (Note that due to the horizontal periodicity and the incompressible assumption for the air, the horizontal average and the time average of H are equivalent, which is written as $\overline{H}$ in this paper.) We consider the sea surface being characterized by a swell wave train and a background broadband wind-sea field that obeys the JONSWAP wave spectrum [45]. The swell wave train propagates in the x-direction, with the crests and troughs parallel to the y-direction (Fig. 1b). Its wave form and motion are described by the high-order Stokes wave solution [46].

Note that swells are long-crest, long-wavelength waves that are generated by distant storms and propagate into the local wind–wave field. Swells from the same storm with different wavelengths (thus with different phase speeds according to the wave dispersion relation) arrive at the offshore wind farm site at different times, with an interval of $O(10)$ hours or even more depending on the distance of the storm [6]. Therefore, for the time duration of $O(1)$ hours for the simulations considered in this study, it is reasonable to assume the swell to be a monochromatic wave train.

Here, we consider nine swell waves within the periodic computational domain, which corresponds to a swell wavelength of $\lambda_s = 233.3$ m. The swell propagates in the downwind direction, which has been investigated much more than other propagation directions in previous studies of wind–wave interaction [e.g. Refs. [8–10,30]], and we follow this choice of canonical problem. Also, within the length scale of offshore wind farms, the dissipation of swell amplitude is negligible. Thus we consider a constant and moderate steepness $2\pi a_s/\lambda_s = 0.1$ that has been used in several previous simulations [4,9,27–29] corresponding to a swell amplitude of $a_s = 3.7$ m. The key parameters of the swell and the JONSWAP wind-sea field are listed in Table 1. For the HOSM, a number of grid points $N_x \times N_y = 512 \times 384$ is used. For the simulation of JONSWAP waves, HOSM was shown to achieve good grid

Table 1
Parameters of wave field for the HOSM simulations. Here, λ is the wavelength; k is the wavenumber; a is the wave amplitude; f is the wave frequency; T is the wave period; and c is the wave phase speed. For the JONSWAP wave field, the listed values correspond to the peak wave mode in the spectrum.

Wave	λ (m)	k (m^{-1})	a (m)	ak	f (s^{-1})	T (s)	c (m/s)
Swell	233.3	0.027	3.7	0.1	0.082	12.2	19.1
JONSWAP	60	0.105	1.0	0.1	0.161	6.2	9.7

resolution independence when more than eight grid points per peak wavelength are used (see Fig. 8 in Xiao et al. [42]). In the current wave simulation, the HOSM uses 15 grid points per peak JONSWAP wavelength and 56 grid points per swell wavelength, sufficient to resolve the energy-containing wave modes in the wave field.

For the LES of offshore wind farms, we consider a 3×3 wind turbine array within the simulation domain, which is a periodic representation of a large wind farm under fully developed condition. In this study we consider the aligned turbine array, which has been used as the baseline case in many previous LES studies [15,19–24]. We note that other turbine arrangements (e.g. staggered and oblique arrays) have also been studied and are found to have noticeable effect on the wind farm performance [19,23,24]. Nevertheless, the focus of this study is the swell effect, which is expected to hold for different turbine layout patterns because the distortion effect of the swell on the wind field is expected to be similar. Therefore, as the first step of swell effect study, we focus on aligned turbine array and leave other arrangements for future investigations. The wind turbines have a hub height of $H_{\rm hub} = 100$ m and a rotor diameter of $D = 100$ m. This leads to a streamwise wind turbine spacing parameter $s_x = (L_x/3)/D = 7.0$ and a spanwise spacing parameter $s_y = (L_y/3)/D = 5.0$.

We note that with respect to the number of wind turbines in the periodic computational domain, which corresponds to a subset of an infinitely large wind farm, both larger (e.g. Calaf et al. [15]) and smaller (e.g. Lu and Porté-Agel [20]) numbers of turbines have been used in previous LES studies and they all showed satisfactory results. The current wind turbine array configuration and simulation domain size have been used in Yang et al. [16]. Comparison with the theoretical solution of wind turbine array boundary layer by Calaf et al. [15] showed excellent agreement, indicating that the current LES configuration is able to capture the essential flow physics of a fully developed wind turbine array boundary layer. Finally, we remark that if a developing turbine array boundary layer is simulated instead of a fully developed one, more turbine rows need to be considered in the streamwise direction to properly capture the downwind development of the flow field [47].

In this study, we consider three different wind conditions. In the simulation, the wind field is driven by an imposed streamwise pressure gradient $\partial p_\infty/\partial x$ (see Section 2.1), and a statistically steady state of the wind field is achieved when the imposed pressure forcing, wind turbine drag, and sea-surface stress reach a balance. At the initial stage of each simulation, we use a relaxation procedure, during which the value of $\partial p_\infty/\partial x$ is tuned so that the mean wind speeds at the top of the simulation domain ($z = 1$ km) obtained from the simulation are close to the desired values of $U_{\rm top} = 7.0$, 10.0, and 17.0 m/s (the exact values obtained from the LES results are given in Table 2), respectively. After the initial relaxation process, the simulations are then carried on and data are collected for statistical analysis. Similar relaxation approach has been used in Yang et al. [16] for LES of offshore wind farms with various turbine spacings in the absence of swells. Based on the values of $\partial p_\infty/\partial x$, the corresponding friction velocities above the turbine array are given by $u_* = \sqrt{-\overline{H}(\partial p_\infty/\partial x)/\rho_a}$, and have the values of $u_* = 0.45$, 0.64, and 1.21 m/s, respectively.

The bottom of the wind field is bounded by sea-surface waves and has a prescribed value of 2.0×10^{-4} m for the subgrid-scale sea-surface roughness z_0, consistent with typical observed values [4,9]. The key parameters for the LES are given in Table 2. Note that in cases J-17 and SJ-17, due to the strong wind, the wave-induced motions are relatively weak compared with those in the other cases. As a result, the wave effect can penetrate less into the wind field. To ensure sufficient vertical resolution to capture the wave effect, we double the vertical grid number for these two cases [16]. The grid resolution used in the current LES is comparable to or higher than previous LES of wind farms [15,19,21,22]. It was shown to be able to capture the essential flow physics in the offshore wind turbine array boundary layer [16].

Table 2
Parameters of LES of offshore wind farm.

Case	Wave condition	$U_{\rm top}$ (m/s)	u_* (m/s)	(N_x,N_y,N_z)	Δt (s)
J-7	JONSWAP	7.0	0.45	(192,128,96)	0.14
SJ-7	Swell + JONSWAP	7.0	0.45	(192,128,96)	0.12
J-10	JONSWAP	10.1	0.64	(192,128,96)	0.14
SJ-10	Swell + JONSWAP	10.0	0.64	(192,128,96)	0.12
J-17	JONSWAP	17.3	1.21	(192,128,192)	0.07
SJ-17	Swell + JONSWAP	17.2	1.21	(192,128,192)	0.06

3. Results

3.1. Effect of swell on extracted wind power

For the study of offshore wind farm dynamics, a key quantity to investigate is the power extraction rate of the wind farm. Based on the LES results, the power extracted by the wind turbines can be calculated directly with the turbine-induced force and wind velocity (assuming a constant relationship between the fluid mechanical power extracted from the fluid and the turbine power). Following Calaf et al. [15], the extracted power density by an individual wind turbine is [15] calculated as

$$P_{q,r} = \frac{\left(\frac{1}{2}C_T'\frac{\pi}{4}D^2\langle u^T\rangle_d^3\right)_{q,r}}{s_x s_y D^2}, \tag{17}$$

where the subscript '(q,r)' denotes the turbine at the q-th row and r-th column. The extracted wind power density averaged among the turbines is then

$$P_T = \frac{1}{N_{\rm row}N_{\rm col}}\sum_{q=1}^{N_{\rm row}}\sum_{r=1}^{N_{\rm col}} P_{q,r}. \tag{18}$$

Fig. 2 shows the time series of P_T for cases J-10 and SJ-10. Similar to the cases of land-based wind farms, P_T for offshore wind farms over a broadband wave field (see case J-10 in Fig. 2a) shows multiscale fluctuations with moderate amplitudes due to the wind turbulence [15,16,19]. Differently, when a swell is present (Fig. 2b), the strong wave motions induce a fluctuation with much higher amplitude than that induced by turbulence only. A zoom-in view for case SJ-10 in Fig. 3 shows that such large temporal fluctuations oscillate at the swell frequency and depend on the wave phase of the swell. Particularly, maxima in P_T are observed when swell troughs arrive beneath the wind turbines, while minima of P_T are observed when swell crests arrive.

These results show that swell-induced oscillations can reduce the power quality of offshore wind farms as well as induce fatigue loads to the wind turbine structure [31,48]. To further quantify the characteristics of the swell-induced oscillations, we sample the time series of P_T from 80,000 continuous timesteps and perform a spectral analysis on these samples. First, all the 80,000 sampling points are taken for a single Fourier transform. The relative magnitude of each Fourier mode with respect to the mean value (i.e. the zero Fourier mode) is $|\widehat{P}_T(f)|/|\widehat{P}_T(f=0)|$, where $\widehat{P}_T(f)$ is the corresponding Fourier mode of P_T at frequency f and $|\cdot|$ indicates its norm. As shown in Fig. 4, despite the noise especially at the high frequency tail, a dominant and highly narrow-banded

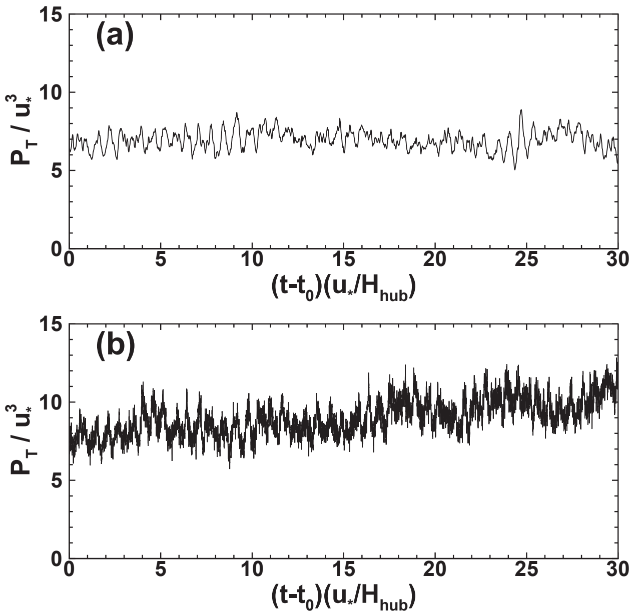

Fig. 2. Time series of the averaged extracted power density of the offshore wind farm for cases (a) J-10 and (b) SJ-10. Here, u_* is the friction velocity for the wind above the turbine array; t_0 is the time when the statistical sampling starts; and H_{hub} is the turbine hub height.

peak is observed at the swell frequency f_s in cases SJ-7 and SJ-10. Particularly, $|\widehat{P}_T(f_s)|/|\widehat{P}_T(f=0)| = 6.7\%$ in case SJ-7 and 4.0% in case SJ-10. This peak at the swell frequency is consistent with the oscillation in the time series of P_T shown in Fig. 3. On the other hand, Fig. 4c for case SJ-17 does not show a swell-induced peak, suggesting that the swell-induced disturbance to the wind is relatively weak under the high wind condition and the fluctuations in P_T are dominated by the wind turbulence.

Next, we take samples of P_T for every 800 continuous timesteps, and then perform ensemble averaging over 100 such temporal sampling windows. This results in a smooth frequency spectrum of P_T. Fig. 5 shows all of the six LES cases. Consistently, a dominant peak at the swell frequency f_s is observed in cases SJ-7 and SJ-10, while no evident swell-induced oscillation is observed in case SJ-17. Moreover, in cases SJ-7 and SJ-10, small but non-negligible peaks at harmonics of the swell frequency are observed. The overall levels of fluctuations at high frequencies $f/f_s > 1$ are also found to be larger in cases SJ-7 and SJ-10 than those in the corresponding swell-absent cases J-7 and J-10 (Fig. 5b and c), consistent with the observations of the time series of P_T shown in Fig. 2.

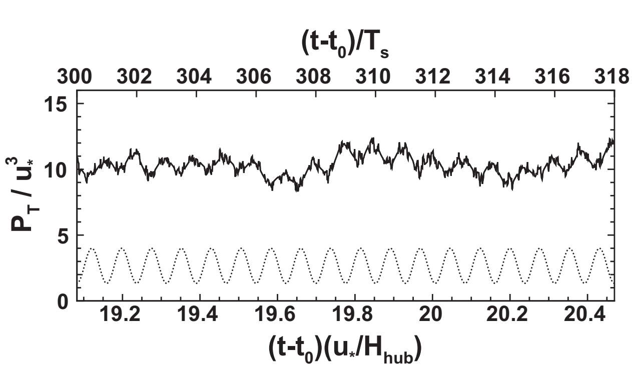

Fig. 3. Zoom-in view of Fig. 2(b) for case SJ-10. Here, the dimensionless time normalized by both the turbulence time scale H_{hub}/u_* and the swell period T_s are shown. The corresponding wave phase of the swell is also indicated by the dotted line at the bottom. (For illustration purpose, the amplitude of the swell is not plotted to scale.)

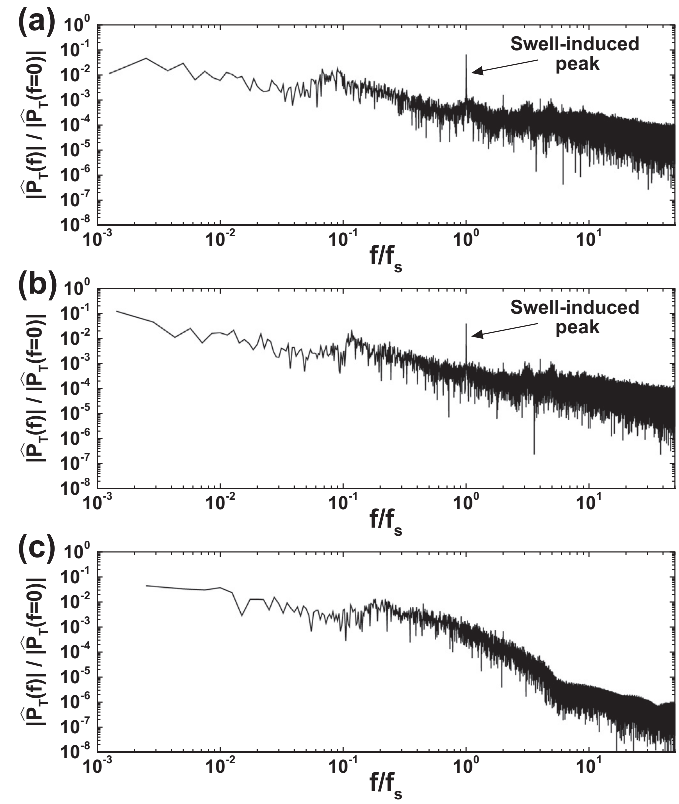

Fig. 4. Relative contribution of extracted wind power at each frequency with respect to the mean value for the swell-present cases of (a) SJ-7, (b) SJ-10 and (c) SJ-17. The values of P_T from 80,000 continuous timesteps are sampled and Fourier transformed. The plotted values are the norm of the Fourier mode $|\widehat{P}_T|$ at each frequency f normalized by the norm at zero frequency (i.e. the mean value).

Swells not only cause large oscillations in the instantaneous wind power output, but also affect the wind farm performance in an averaged sense. Fig. 6 shows the value of $\overline{P}_T$ (the overbar denotes time-averaging). For all of the cases considered in this study, the dimensionless value $\overline{P}_T/u_*^3$ has the same order of magnitude as those for land-based wind farms obtained by LES [15]. The values in the current offshore cases do appear higher than those in the land-based cases ($\overline{P}_T/u_*^3 \sim 5.0$ [15]) as expected due to the much smaller surface roughness at the sea than on the land. The comparisons of $\overline{P}_T$ between cases SJ-7 and J-7 and between cases SJ-10 and J-10 show that the presence of downwind swells causes an increase in $\overline{P}_T$. When the wind becomes stronger, comparison between cases SJ-17 and J-17 shows that the effect of swell on $\overline{P}_T$ diminishes, similar to the observations made about the temporal oscillations (Figs. 4c and 5c).

Previous studies on wind–wave interaction showed that the effect of surface wave motions on the turbulence statistics can be characterized by wave age, which is defined as the ratio of wave phase speed to a characteristic wind velocity (e.g. the wind friction velocity u_*) [2,4]. Similarly, the wave age of a swell can be defined as c_s/u_*, where c_s is the phase speed of the swell. Fig. 7 shows that, as the swell wave age c_s/u_* increases, the swell-induced relative increment of $\overline{P}_T$ also increases, from 1.7% at $c_s/u_* = 15.8$ to 13.6% at $c_s/u_* = 29.8$, and to 18.8% at $c_s/u_* = 42.4$.

3.2. Effect of swell on flow statistics of the wind turbine array boundary layer

To help understand the mechanisms of swell effect on wind turbine performance, we study the statistics of the turbulent flow

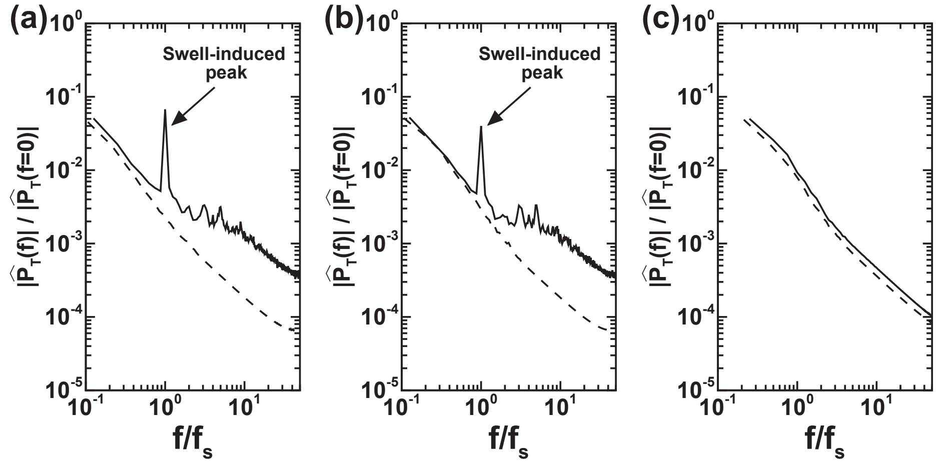

Fig. 5. Relative contribution of extracted wind power at each frequency with respect to the mean value for various cases: (a) J-7 (dashed line) and SJ-7 (solid line); (b) J-10 (dashed line) and SJ-10 (solid line); and (c) J-17 (dashed line) and SJ-17 (solid line). The values of P_T from 80,000 continuous timesteps are sampled in a sampling window of every 800 timesteps, Fourier transformed, and then averaged over the 100 sampling windows. The plotted values are the norm of the Fourier mode $|\hat{P}_T|$ at each frequency f normalized by the norm at zero frequency (i.e. the mean value).

field in the offshore wind turbine array boundary layer. First, we calculate the swell phase-averaged value of the streamwise velocity u by performing ensemble averaging of instantaneous three-dimensional LES data of the same phase with respect to the swell. The swell phase-averaged quantity of a variable f is denoted as $\langle f\rangle_p$. The corresponding phase-dependent fluctuation is $f_p' = f_p - \langle f\rangle_p$, where f_p is the instantaneous value of f at the given swell phase. Note that for the simulation cases without swell, the phase average reduces to the usual time average, which is denoted by overbar $\overline{f}$ as defined earlier, and the phase-dependent fluctuation f_p' also reduces to the temporal fluctuation $f' = f - \overline{f}$.

Fig. 8 shows the swell phase-averaged streamwise velocity $\langle u\rangle_p$ on the (x,z)-plane along the center of the wind turbine. For cases SJ-7 and SJ-10, the contours of $\langle u\rangle_p$ show apparent dependence on the swell phase. Particularly, $\langle u\rangle_p$ has relatively large value above the trough of the swell but small value above the crest, consistent with previous LES of wind over swells [9]. For case SJ-17, which has stronger wind, the swell-induced variation on $\langle u\rangle_p$ is weak. As a comparison, case J-10 that is without swell is also plotted. The result shows more uniform distribution of $\langle u\rangle_p$ close to the almost flat mean sea surface, because the effects of the small waves in the broadband wave field are averaged out.

Furthermore, we take the profiles of $\langle u\rangle_p$ along the vertical centerline 0.2D in front of the wind turbine disk and plot them in Fig. 9. For case SJ-7 (Fig. 9a), $\langle u\rangle_p$ is high at the swell-trough phase and low at the swell-crest phase; the profile of the swell-absent case J-7 falls between the two profiles of case SJ-7. Such swell-induced variation is found to extend vertically to the wind turbine rotor height. Consequently, the disk-averaged velocity $\langle u^T\rangle_d$ also experiences similar swell-induced variation, causing P_T to vary with the swell phase (because $P_T \propto \langle u^T\rangle_d^3$ as indicated by Eqs. (17) and (18)). Similar but relatively weak swell effect on the vertical profiles of $\langle u\rangle_p$ is also observed in case SJ-10 (Fig. 9b). The swell effect further reduces when the wind speed increases to $U_{\rm top} = 17$ m/s, as indicated by the much smaller difference between cases SJ-17 and J-17 (Fig. 9c).

Moreover, Fig. 9a and b also show that above the swell trough, there exists a swell-induced acceleration in the mean streamwise velocity profile between the turbine disk and the wave surface. Observations of wave-driven wind have been reported recently in various studies of wind–wave interacting flows [8–10], where the

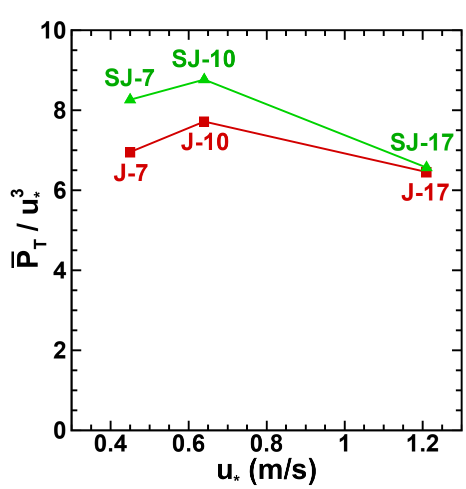

Fig. 6. Time-averaged extracted power density of the offshore wind farm as a function of u_*. Cases without the presence of swells are indicated by ■; cases with swells are indicated by ▲.

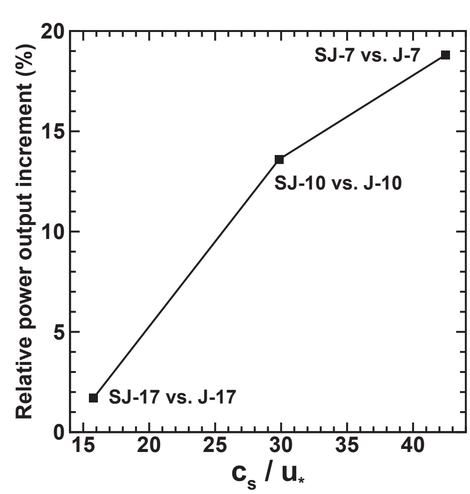

Fig. 7. Relative swell-induced increment of mean extracted wind power (with respect to the corresponding swell-absent case) as a function of swell wave age c_s/u_*.

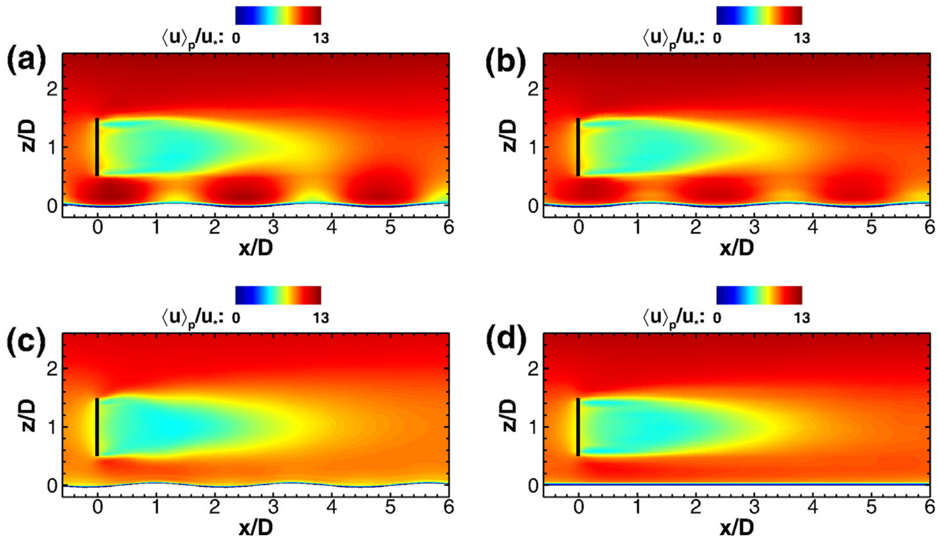

Fig. 8. Swell phase-averaged streamwise velocity $\langle u\rangle_p$ on the (x,z)-plane across the center of the wind turbine. Results for the three swell-present cases are shown: (a) SJ-7; (b) SJ-10; and (c) SJ-17. At the selected phase, the trough of the swell arrives at the wind turbine location. The swell-absent case J-10 is shown in (d) for comparison. The location of the turbine disk is indicated by the thick vertical line.

waves propagate faster than the wind and induce strong wave forcing to the lower portion of the wind field. Regarding wind energy harvesting, fast-propagating waves can feed energy back to the wind field to increase the extracted wind power (Fig. 7).

Figs. 10–12 show the swell phase-averaged velocity variances $\langle u'_p u'_p\rangle_p, \langle w'_p w'_p\rangle_p$, and Reynolds stress $\langle -u'_p w'_p\rangle_p$, respectively. Typical wind turbine wake structures are observed, i.e. large $\langle u'_p u'_p\rangle_p$ at the upper and lower edges of the turbine wake, large

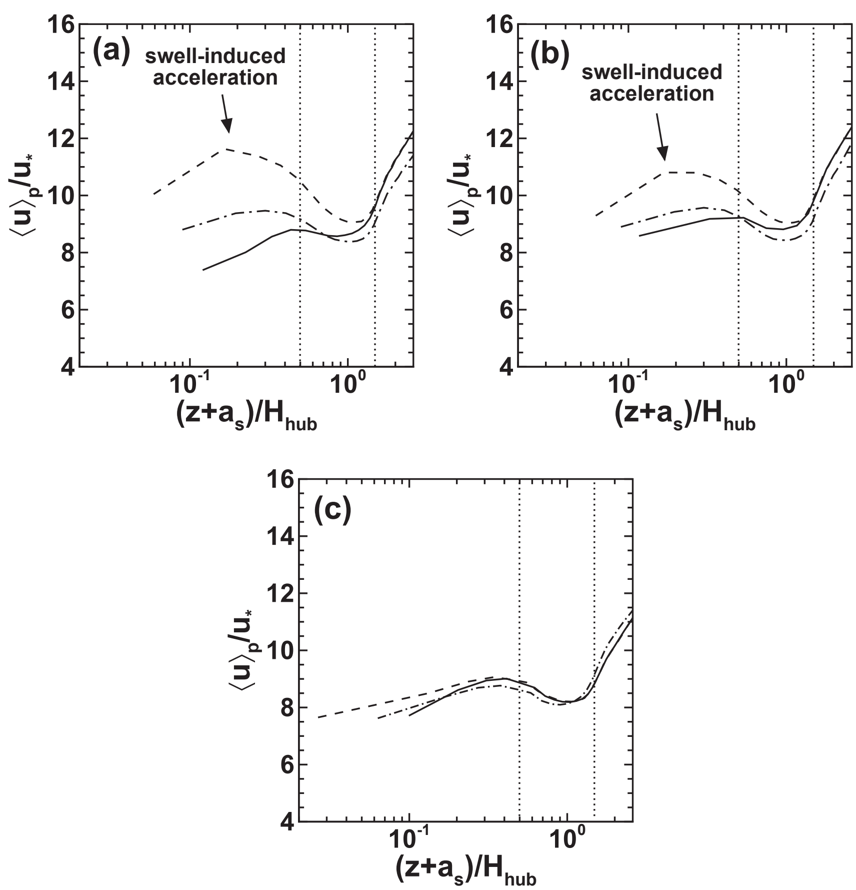

Fig. 9. Profiles of swell phase-averaged streamwise velocity along the vertical centerline 0.2D in front of the wind turbine: (a) cases SJ-7 and J-7; (b) cases SJ-10 and J-10; and (c) cases SJ-17 and J-17. In each swell case, the profiles at two phases are plotted: – – –, the swell trough arrives at the wind turbine location; ———, the swell crest arrives at the wind turbine location. The profiles for the swell-absent cases are indicated by – • –. The lower and upper edges of the wind turbine disk are indicated by the two dotted lines.

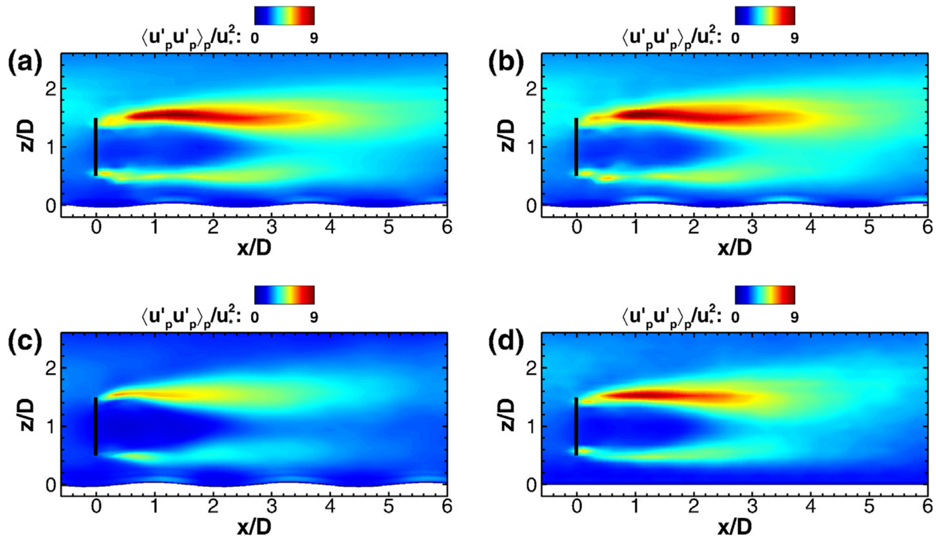

Fig. 10. Swell phase-averaged streamwise velocity variance $\langle u'_p u'_p \rangle_p$ on the (x,z)-plane across the center of the wind turbine. Results for the three swell-present cases are shown: (a) SJ-7; (b) SJ-10; and (c) SJ-17. At the selected phase, the trough of the swell arrives at the wind turbine location. The swell-absent case J-10 is shown in (d) for comparison. The location of the turbine disk is indicated by the thick vertical line.

$\langle w'_p w'_p \rangle_p$ within the turbine wake, as well as positive and negative $\langle -u'_p w'_p \rangle_p$ at the upper and lower edges of the wake, respectively. These general features are consistent with the laboratory measurements of wind turbine wake flow [49,50].

Consistent with the streamwise velocity (Fig. 8), Figs. 10–12 also show apparent swell effect on the velocity variances and Reynolds stress, especially for cases SJ-7 and SJ-10. The swell motions induce strong distortion to the lower portion of the wind field, enhancing both the streamwise and vertical turbulent fluctuations above the swell crests (Fig. 10a and b, as well as Fig. 11a and b). Meanwhile, because of the swell-enhanced wind velocity in the near surface region, the swell-present case SJ-10 shows larger values than the swell-absent case J-10 for both the streamwise velocity variance (Fig. 10b versus Fig. 10d) and the Reynolds stress (Fig. 12b versus Fig. 12d).

We remark that in a large wind farm, except for the wind turbines in the first front rows, most of the wind turbines are located in the wakes of other turbines. Therefore, a key factor that determines the overall performance of a wind farm is the recovery rate of the wind velocity in the turbine wake. Calaf et al. [15] showed that a large land-based wind farm gains energy to recover to the nominal wind speed mainly by the vertical flux of kinetic energy from the atmosphere above. Yang et al. [16] showed that similar mechanism also dominates in offshore wind farms if the sea surface has a broadband wave field of moderate amplitudes. The swell-enhanced turbulent mixing in the wind turbine wake (Figs. 10–12) is expected to make further contribution to the recovery of wind energy in the wake region.

Here, we perform analysis of horizontally averaged mean kinetic energy budget in a way similar to Calaf et al. [15] to understand the swell-induced enhancement of wind farm performance in cases SJ-7 and SJ-10 shown in Section 3.1. The net kinetic energy flux into the wind rotor layers of the flow can be evaluated as

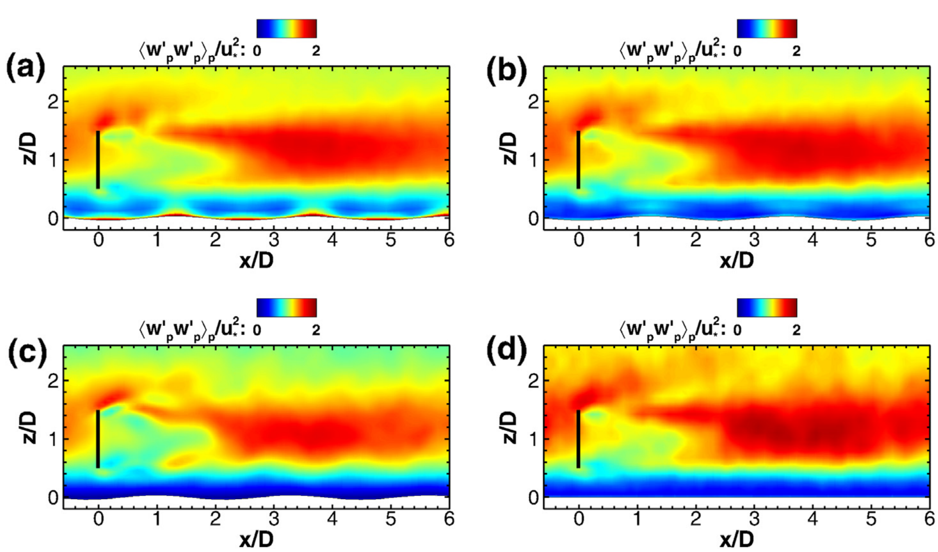

Fig. 11. Swell phase-averaged vertical velocity variance $\langle w'_p w'_p \rangle_p$ on the (x,z)-plane across the center of the wind turbine. Results for the three swell-present cases are shown: (a) SJ-7; (b) SJ-10; and (c) SJ-17. At the selected phase, the trough of the swell arrives at the wind turbine location. The swell-absent case J-10 is shown in (d) for comparison. The location of the turbine disk is indicated by the thick vertical line.

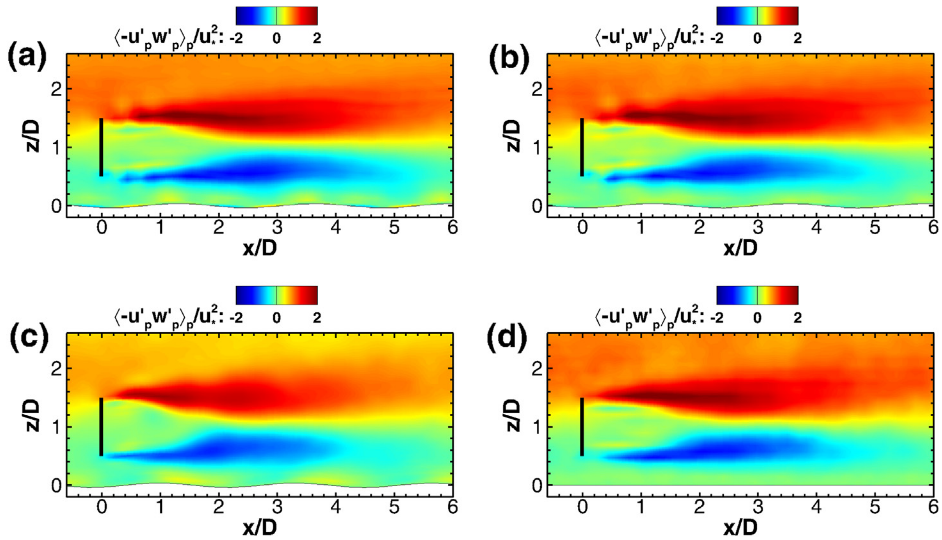

Fig. 12. Swell phase-averaged Reynolds stress $\langle -u'_p w'_p \rangle_p$ on the (*x*,*z*)-plane across the center of the wind turbine. Results for the three swell-present cases are shown: (a) SJ-7; (b) SJ-10; and (c) SJ-17. At the selected phase, the trough of the swell arrives at the wind turbine location. The swell-absent case J-10 is shown in (d) for comparison. The location of the turbine disk is indicated by the thick vertical line.

$$\Delta\Phi_e = \Big(\underbrace{-\langle \overline{u'w'} \rangle \langle \overline{u} \rangle}_{\Phi_e^R} \ \underbrace{-\langle \overline{u}''\overline{w}'' \rangle \langle \overline{u} \rangle}_{\Phi_e^d} \Big) \Big|_{z/\overline{H}=0.05}^{z/\overline{H}=0.15}. \quad (19)$$

Here, the brackets $\langle\cdot\rangle$ denote horizontal averaging (as opposed to phase averaging introduced earlier); and $u_i'' = u_i - \langle \overline{u}_i \rangle$ denotes the fluctuating velocity due to both temporal and spatial variations. In Eq. (19), the first term on the right-hand side, Φ_e^R, represents the contribution from the Reynolds shear stress $-\langle \overline{u'w'} \rangle$. The second term, Φ_e^d, represents the contribution from the dispersive shear stress $-\langle \overline{u}''\overline{w}'' \rangle$, which indicates the correlation between the spatial inhomogeneities of $\overline{u}$ and $\overline{w}$ [51].

Fig. 13 shows the vertical profiles of the mean streamwise velocity $\langle \overline{u} \rangle$. Both swell-present cases SJ-7 and SJ-10 show larger wind velocity than the corresponding swell-absent cases J-7 and J-10. Fig. 14 shows the vertical profiles of the stress components. Similar to the results of land-based wind farms [15], the Reynolds stress also dominates in the offshore wind farm considered in this study, with small but non-negligible contribution from the dispersive stress. When added together, the total stress profile is obtained. As $z/\overline{H}$ decreases from 1 to 0, the total stress increases linearly up to the top of the wind turbine region, and then decreases rapidly over the turbine rotor region ($0.05 \le z/\overline{H} \le 0.15$) due to the horizontally averaged momentum extraction by the wind turbines. We note that in Fig. 14 the dispersive stress has a noticeable value at high elevation above the wind turbines, i.e. at $0.2 \le z/\overline{H} \le 0.6$. Different from other types of canopy flows, such as flows over plant forest [52] and urban buildings [53], wind turbines are deployed relatively far from each other, allowing the turbine wakes to interact with the atmospheric boundary layer more and induce considerable spatial variations that extend to high elevation, resulting in non-negligible dispersive stress. Similar results have been reported in previous studies of wind turbine array boundary layer [15,16,22]. Those studies also showed that the magnitude of the high-elevation dispersive stress may vary (roughly between 0.1 and 0.2 when normalized by u_*^2) depending on the number of snapshots for statistical analysis and the details of different LES models, but the dispersive stress near and within the turbine rotor region is found to be much less sensitive and is usually well captured [16,22].

An interesting and important phenomenon in cases SJ-7 and SJ-10 is that the Reynolds stress is negative at the lower edge of the

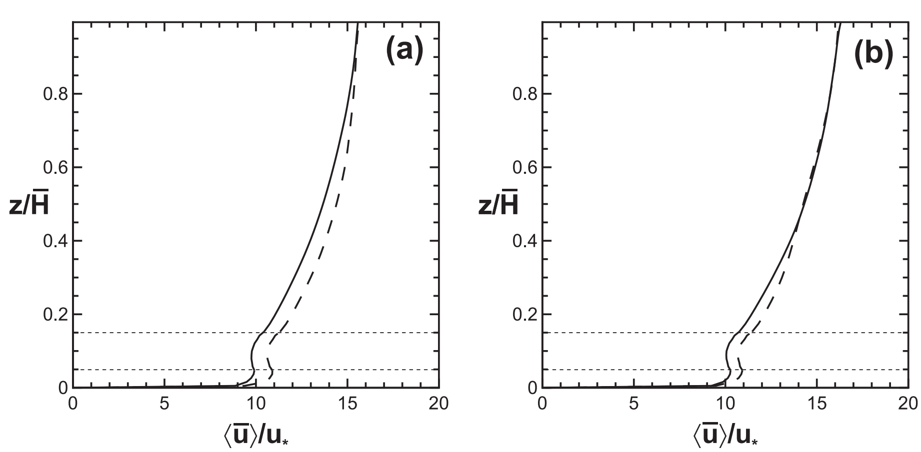

Fig. 13. Vertical profiles of mean streamwise velocity $\langle \overline{u} \rangle$ for various cases: (a) J-7 (—) and SJ-7 (– – –); and (b) J-10 (—) and SJ-10 (– – –).

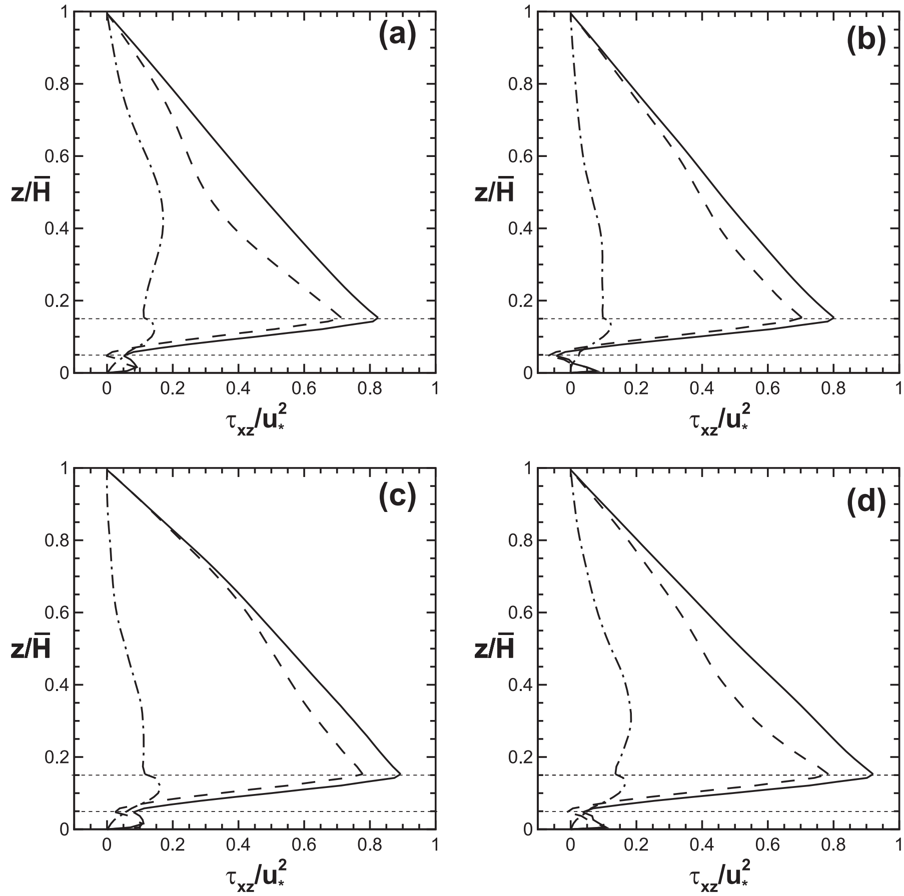

Fig. 14. Comparison of the stress profiles: — — —, Reynolds stress $-\langle \overline{u'w'} \rangle$; —·—, dispersive stress $-\langle \overline{u}''\overline{w}'' \rangle$; and ———, total stress. Results from various cases are shown: (a) J-7; (b) SJ-7; (c) J-10; and (d) SJ-10.

turbine rotor region ($z/\overline{H} = 0.05$), i.e. $-\langle \overline{u'w'} \rangle / u_*^2 = -0.07$ for SJ-7 (Fig. 14b) and -0.01 for SJ-10 (Fig. 14d). Note that previous studies showed that the velocity profile has a negative slope on the lower edge of the wake behind the wind turbine, thus results in a negative sign for $-u'w'$ there [14,54,55]. Outside the turbine wake, however, $-u'w'$ is dominated by positive values similar to usual turbulence boundary layer. When calculating $-\langle \overline{u'w'} \rangle$, averaging over the entire horizontal plane is performed. Therefore, for cases J-7 and J-10, the overall result is that $-\langle \overline{u'w'} \rangle > 0$ at $z/\overline{H} = 0.05$ (see e.g. Fig. 14a and c, and Ref. [15]).

Different from cases J-7 and J-10, for cases SJ-7 and SJ-10 the swell-induced wind acceleration increases the negative slope of the mean velocity profile at the lower edge of the turbine wake, particularly above the swell trough (Fig. 9a and b). Consequently, the contributions from the negative $-u'w'$ are large enough to result in $-\langle \overline{u'w'} \rangle < 0$ at $z/\overline{H} = 0.05$ after horizontal averaging. This negative Reynolds stress results in $\Phi_e^R < 0$ at $z/\overline{H} = 0.05$, leading to an upward flux of kinetic energy into the turbine rotor wake from the near-wave region (see Eq. (19)). The values for cases SJ-7 and SJ-10 are listed in Table 3. Moreover, due to the larger wind speed in the swell-present cases than in the corresponding swell-absent cases, the energy flux at $z/\overline{H} = 0.15$ is larger in cases SJ-7 and SJ-10 than in cases J-7 and J-10, respectively, as shown in Table 3. The combined effects of negative Φ_e^R at $z/\overline{H} = 0.05$ and enhanced Φ_e^R at $z/\overline{H} = 0.15$ lead to a larger net energy flux $\Delta\Phi_e^R$ when the swell is present. The relative increment of $\Delta\Phi_e^R$ is 15.8% between cases SJ-7 and J-7, and is 12.4% between cases SJ-10 and J-10. These values are comparable to the corresponding relative increment of extracted wind power shown in Fig. 7.

Table 3
Reynolds stress induced kinetic energy flux for moderate wind cases. The values in the table have been normalized by u_*^3.

Case	$\Phi_e^R\big\vert_{z/\overline{H}=0.15}$	$\Phi_e^R\big\vert_{z/\overline{H}=0.15}$	$\Delta\Phi_e^R$
J-7	7.34	0.02	7.32
SJ-7	7.80	−0.68	8.48
J-10	8.19	0.29	7.90
SJ-10	8.82	−0.07	8.89

4. Conclusions

Generated by distant storms, ocean swells can travel over large distances with limited decay in their amplitudes, enter the offshore wind farm sites, and induce considerable impact on the local wind field [3,5–7]. In this study, the effect of a moderate downwind swell with $(a_s, \lambda_s) = (3.7\ \text{m}, 233.3\ \text{m})$ on the performance of offshore wind farm has been studied numerically under both moderate ($U_{top} = 7.0$ and 10.0 m/s) and relatively high ($U_{top} = 17.0$ m/s) wind conditions.

In order to directly capture the interaction between the offshore wind turbine array boundary layer and the swell-present wave field, a recently developed hybrid numerical tool is adopted [16]. A suite of simulations have been performed, with a swell-present case and a reference swell-absent case for each wind condition. Although not obvious under the relatively high wind condition, under moderate wind condition considerable effects of the swell on the wind energy harvesting have been found. Particularly, when the swell is present, a temporal oscillation of extracted wind power appears at the swell frequency, with a relative magnitude of 4.0% of the mean power output for $U_{top} = 10.0$ m/s and 6.7% for $U_{top} = 7.0$ m/s. Statistical analysis using the phase-averaging approach based on the swell phase indicates that such oscillations are caused by the swell-induced periodic variations in the lower atmospheric boundary layer, with high wind speed above the swell trough and low wind speed above the swell crest.

In addition, the mean value of the extracted wind power is also found to be affected noticeably by the swell for the moderate wind conditions. A swell-induced increment of 13.6% relative to the mean value of the reference swell-absent case is found for $U_{top} = 10.0$ m/s, and 18.9% for $U_{top} = 7.0$ m/s. Temporal- and horizontal-averaged profiles of wind speed and vertical kinetic energy flux suggest that it is the swell-induced flow acceleration in the wind field that is responsible for the increase of mean wind speed as well as the generation of an upward kinetic energy flux into the wind turbine layer, resulting in the wind power increment.

Finally, we remark that this study is a first attempt on the investigation of the swell effect on wind farms. We have focused on the canonical problem of the effect of a downwind swell on an aligned and stably moored wind turbine array. To obtain a more complete picture of the complex flow physics for offshore wind farms under various conditions, follow-up studies on other factors need to be performed. Examples include variations in swell wavelength and amplitude, relatively large oscillating motions when less stable turbine platforms are used, more complex wind farm layout (e.g. oblique and staggered turbine arrangement), and misalignment between wind and swell propagation directions. These effects are beyond the scope of this paper, but should be the subjects of future studies.

Acknowledgments

DY and LS acknowledge the support of NSF-CBET-1341062 on the wind energy study and the support of ONR on some of the development of the wind–wave simulation tool. CM acknowledges the support of NSF-AGS-1045189 and NSF-OISE-1243482.

References

[1] Donelan MA. Air–sea interaction. In: LeMehaute B, Hanes DM, editors. The sea, vol. 9. Wiley-Interscience; 1990. pp. 239–92.
[2] Belcher SE, Hunt JCR. Turbulent flow over hills and waves. Annu Rev Fluid Mech 1998;30:507–38.
[3] Edson J, Crawford T, Crescenti J, Farrar T, Frew N, Gerbi G, et al. The coupled boundary layers and air–sea transfer experiment in low winds. Bull Am Meteor Soc 2007;88:341–56.
[4] Sullivan PP, McWilliams JC. Dynamics of winds and currents coupled to surface waves. Annu Rev Fluid Mech 2010;42:19–42.
[5] Dobson FW, Smith SD, Anderson RJ. Measuring the relationship between wind stress and sea state in the open ocean in the presence of swell. Atmos Ocean 1994;32:237–56.
[6] Donelan MA, Drennan WM, Katsaros KB. The air–sea momentum flux in conditions of wind sea and swell. J Phys Oceanogr 1997;27:2087–99.
[7] Smedman A, Högström U, Bergström H, Rutgersson A, Kahma KK, Petersson H. A case study of air–sea interaction during swell conditions. J Geophys Res 1999;104:25833–51.
[8] Hanley KE, Belcher SE. Wave-driven wind jets in the marine atmospheric boundary layer. J Atmos Sci 2008;65:2646–60.
[9] Sullivan PP, Edson JE, Hristov T, McWilliams JC. Large-eddy simulations and observations of atmospheric marine boundary layers above nonequilibrium surface waves. J Atmos Sci 2008;65:1225–45.
[10] Semedo A, Saetra Ø, Rutgersson A, Kahma KK, Pettersson H. Wave-induced wind in the marine boundary layer. J Atmos Sci 2009;66:2256–71.
[11] Jimenez A, Crespo A, Migoya E, Garcia J. Advances in large-eddy simulation of a wind turbine wake. J Phys Conf Ser 2007;75:012041.
[12] Jimenez A, Crespo A, Migoya E, Garcia J. Large-eddy simulation of spectral coherence in a wind turbine wake. Environ Res Lett 2008;3:015004.
[13] Troldborg N, Sorensen JN, Mikkelsen R. Numerical simulations of wake characteristics of a wind turbine in uniform inflow. Wind Energy 2010;13:86–99.
[14] Wu Y-T, Porté-Agel F. Large-eddy simulation of wind-turbine wakes: evaluation of turbine parametrisations. Boundary-Layer Meteorol 2011;138:345–66.
[15] Calaf M, Meneveau C, Meyers J. Large eddy simulation study of fully developed wind-turbine array boundary layers. Phys Fluids 2010;22:015110.
[16] Yang D, Meneveau C, Shen L. Large-eddy simulation of offshore wind farm. Phys Fluids 2014;26:025101.
[17] Yang D, Shen L. Simulation of viscous flows with undulatory boundaries. Part I: Basic solver. J Comput Phys 2011;230:5488–509.
[18] Yang D, Shen L. Simulation of viscous flows with undulatory boundaries. Part II: coupling with other solvers for two-fluid computations. J Comput Phys 2011;230:5510–31.
[19] Meyers J, Meneveau C. Large eddy simulation of large wind-turbine arrays in the atmospheric boundary layer. In: Proceedings of the 48th AIAA aerospace sciences meeting including the new horizons forum and aerospace exposition 2010. AIAA; 2010. p. 827.
[20] Lu H, Porté-Agel F. Large-eddy simulation of a very large wind farm in a stable atmospheric boundary layer. Phys Fluids 2011;23:065101.
[21] Calaf M, Parlange M, Meneveau C. Large eddy simulation study of scalar transport in fully developed wind-turbine array boundary layers. Phys Fluids 2011;23:126603.
[22] Yang X, Kang S, Sotiropoulos F. Computational study and modeling of turbine spacing effects in infinite aligned wind farms. Phys Fluids 2012;24:115107.
[23] Wu Y-T, Porté-Agel F. Simulation of turbulent flow inside and above wind farms: model validation and layout effects. Boundary-Layer Meteorol 2013;146:181–205.
[24] Stevens RJAM, Gayme DF, Meneveau C. Effect of turbine alignment on the average power output of wind-farms. In: Proceedings of the 2013 international conference on aerodynamics of offshore wind energy systems and wakes. Available online at: http://indico.conferences.dtu.dk. p. 611–23.
[25] Wayman EN, Sclavounos PD, Butterfield S, Jonkman J, Musial W. Coupled dynamic modeling of floating wind turbine systems. NREL/CP-500-39481, http://www.nrel.gov/docs/fy06osti/39481.pdf; 2006.
[26] Roddier D, Cermelli C, Aubault A, Weinstein A. WindFloat: a floating foundation for offshore wind turbines. J Renew Sustain Energy 2010;2:033104.
[27] Sullivan PP, McWilliams JC, Moeng C-H. Simulation of turbulent flow over idealized water waves. J Fluid Mech 2000;404:47–85.
[28] Li PY, Xu D, Taylor PA. Numerical modelling of turbulent airflow over water waves. Boundary-Layer Meteorol 2000;95:397–425.
[29] Kihara N, Hanazaki H, Mizuya T, Ueda H. Relationship between airflow at the critical height and momentum transfer to the traveling waves. Phys Fluids 2007;19:015102.
[30] Cohen JE, Belcher SE. Turbulent shear flow over fast-moving waves. J Fluid Mech 1999;386:345–71.
[31] Burton T, Jenkins N, Sharpe D, Bossanyi E. Wind energy handbook. 2nd ed. John Wiley & Sons Ltd; 2011.
[32] Bou-Zeid E, Meneveau C, Parlange M. A scale-dependent lagrangian dynamic model for large eddy simulation of complex turbulent flows. Phys Fluids 2005;17:025105.
[33] Wan F, Porté-Agel F, Stoll R. Evaluation of dynamic subgrid-scale models in large-eddy simulations of neutral turbulent flow over a two-dimensional sinusoidal hill. Atmos Environ 2007;41:2719–28.
[34] Yang D, Shen L. Characteristics of coherent vortical structures in turbulent flows over progressive surface waves. Phys Fluids 2009;21:125106.
[35] Yang D, Shen L. Direct-simulation-based study of turbulent flow over various waving boundaries. J Fluid Mech 2010;650:131–80.
[36] Yang D, Meneveau C, Shen L. Dynamic modelling of sea-surface roughness for large-eddy simulation of wind over ocean wavefield. J Fluid Mech 2013;726:62–99.
[37] Liu Y, Yang D, Guo X, Shen L. Numerical study of pressure forcing of wind on dynamically evolving water waves. Phys Fluids 2010;22:041704.
[38] Dommermuth DG, Yue DKP. A high-order spectral method for the study of nonlinear gravity waves. J Fluid Mech 1987;184:267–88.
[39] Liu Y, Yue DKP. On generalized Bragg scattering of surface waves by bottom ripples. J Fluid Mech 1998;356:297–326.
[40] Alam M-R, Liu Y, Yue DKP. Oblique sub- and super-harmonic Bragg resonance of surface waves by bottom ripples. J Fluid Mech 2010;643:437–47.
[41] Alam M-R, Liu Y, Yue DKP. Attenuation of short surface waves by the sea floor via nonlinear sub-harmonic interaction. J Fluid Mech 2011;689:529–40.
[42] Xiao W, Liu Y, Wu G, Yue DKP. Rogue wave occurrence and dynamics by direct simulations of nonlinear wavefield evolution. J Fluid Mech 2013;720:357–92.
[43] Zakharov VE. Stability of periodic wave of finite amplitude on the surface of a deep fluid. J Appl Mech Tech Phys 1968;2:190–4.
[44] Mei CC, Stiassnie M, Yue DKP. Theory and applications of ocean surface waves. Part 2: Nonlinear aspects. World Sci 2005;23.
[45] Hasselmann K, Barnett TP, Bouws E, Carlson H, Cartwright DE, Enke K, et al. Measurements of wind-wave growth and swell decay during the Joint North Sea Wave Project (JONSWAP). Dtsch Hydrogr Z Suppl 1973;8:N12.
[46] Schwartz LW. Computer extension and analytic continuation of Stokes' expansion for gravity waves. J Fluid Mech 1974;62:553–78.

[47] Stevens RJAM, Graham J, Meneveau C. A concurrent precursor inflow method for large eddy simulations and applications to finite length wind farms. Renew Energy 2014;68:46–50.
[48] Manwell JF, McGowan JG, Rogers AL. Wind energy explained – theory, design and application. 2nd ed. John Wiley & Sons Ltd; 2010.
[49] Vermeer LJ, Sørensen JN, Crespo A. Wind turbine wake aerodynamics. Prog Aerosp Sci 2003;39:467–510.
[50] Zhang W, Markfort CD, Porté-Agel F. Near-wake flow structure downwind of a wind turbine in a turbulent boundary layer. Exp Fluids 2012;52:1219–35.
[51] Raupach MR, Antonia RA, Rajagopalan S. Rough-wall turbulent boundary layers. Appl Mech Rev 1991;44:1–25.
[52] Yue W, Parlange MB, Meneveau C, Zhu W, van Hout R, Katz J. Large-eddy simulation of plant canopy flows using plant-scale representation. Boundary-Layer Meteorol 2007;124:183–203.
[53] Coceal O, Thomas TG, Castro IP, Belcher SE. Mean flow and turbulence statistics over groups of urban-like cubical obstacles. Boundary-Layer Meteorol 2006;121:491–519.
[54] Chamorro LP, Porté-Agel F. Effects of thermal stability and incoming boundary-layer flow characteristics on wind-turbine wakes: a wind-tunnel study. Boundary-Layer Meteorol 2010;136:515–33.
[55] Chamorro LP, Porté-Agel F. Turbulent flow inside and above a wind farm: a wind-tunnel study. Energies 2011;4:1916–36.